

On the Prediction of α -Martensite Temperatures in Medium Manganese Steels



DANIEL M. FIELD, DANIEL S. BAKER, and DAVID C. VAN AKEN

A new composition-based method for calculating the α -martensite start temperature in medium manganese steel is presented and uses a regular solution model to accurately calculate the chemical driving force for α -martensite formation, $\Delta G_{\text{Chem}}^{\gamma \rightarrow \alpha}$. In addition, a compositional relationship for the strain energy contribution during martensitic transformation was developed using measured Young's moduli (E) reported in literature and measured values for steels produced during this investigation. An empirical relationship was developed to calculate Young's modulus using alloy composition and was used where dilatometry literature did not report Young's moduli. A comparison of the $\Delta G_{\text{Chem}}^{\gamma \rightarrow \alpha}$ normalized by dividing by the product of Young's modulus, unconstrained lattice misfit squared (δ^2), and molar volume (Ω) with respect to the measured α -martensite start temperatures, M_S^α , produced a single linear relationship for 42 alloys exhibiting either lath or plate martensite. A temperature-dependent strain energy term was then formulated as $\Delta G_{\text{str}}^{\gamma \rightarrow \alpha}$ (J/mol) = $E\Omega\delta^2(14.8 - 0.013T)$, which opposed the chemical driving force for α -martensite formation. M_S^α was determined at a temperature where $\Delta G_{\text{Chem}}^{\gamma \rightarrow \alpha} + \Delta G_{\text{str}}^{\gamma \rightarrow \alpha} = 0$. The proposed M_S^α model shows an extended temperature range of prediction from 170 K to 820 K (-103 °C to 547 °C). The model is then shown to corroborate alloy chemistries that exhibit two-stage athermal martensitic transformations and two-stage TRIP behavior in three previously reported medium manganese steels. In addition, the model can be used to predict the retained γ -austenite in twelve alloys, containing ε -martensite, using the difference between the calculated M_S^ε and M_S^α .

DOI: 10.1007/s11661-017-4020-2

© The Minerals, Metals & Materials Society and ASM International 2017

I. INTRODUCTION

ACCURATE calculation of martensitic start temperatures (M_S) for steel has been an elusive and important goal in the effort to design new advanced high-strength steels (AHSS) that utilize transformation-induced plasticity (TRIP) behavior to increase ductility and improve crashworthiness of automotive sheet steel. Quench and partitioned steels have shown ultimate tensile strengths in excess of 1500 MPa with elongation to failure of 20 pct,^[1] whereas two-stage TRIP steels have shown strengths in excess of 1200 MPa and elongation to failure greater than 30 pct.^[2-4] Thus, the ability to correctly predict the M_S temperature is important when quench and partitioning is used to develop retained γ -austenite in these new AHSS.^[1,5-7] Likewise, AHSS developed to show two-stage TRIP behavior^[2-4,8,9] where γ -austenite first transforms to ε -martensite and then to α -martensite ($\gamma \rightarrow \varepsilon \rightarrow \alpha$) also requires better models to formulate compositions that obtain the highest level of transformable microstructure, *i.e.*, γ -austenite or ε -martensite. This difficulty is

highlighted by the work of Acet *et al.*^[10] and Holden *et al.*^[11] for medium manganese steels in the range of 10 to 15 at. pct manganese. Figure 1(a) shows that in this compositional range, both α -martensite and ε -martensite are observed, and according to Figure 1(b), a mixed α and ε martensitic structure would occur in the range of 8 to 12 wt pct manganese. Microstructural evolution during γ -austenite transformation is expected to vary depending upon which martensite forms first; thus, accurate prediction of these temperatures is very important.

Manganese, silicon, and aluminum have been important alloying components of TRIP steel despite the lack of fully understanding the compositional dependence on the M_S temperature. For ε -martensite, the start temperature is expected to correlate with the intrinsic stacking fault energy, and manganese shows a parabolic relationship with a minimum predicted in the range of the medium manganese steels.^[12] Manganese is also known for lowering the elastic moduli of steel,^[13] and this may affect the strain energy of formation of α -martensite. Most empirical models for the α -martensite start temperature are derived for low-alloy steel-containing solute contents less than 5 wt pct. In this regard, two empirical models are reported by DeCooman and Speer^[14] which contain aluminum (Eqs. [1] and [2]), and a third model is provided for non-aluminum-containing steels (Eq. [3]) that will be used in this study for steels containing Ni and Cr. As these empirical models show for low-alloy

DANIEL M. FIELD and DAVID C. VAN AKEN are with the Department of Materials Science and Engineering, Missouri University of Science and Technology, Rolla, MO 65409. Contact e-mail: dfb52@mst.edu DANIEL S. BAKER is with General Motors Global Propulsions Systems, Pontiac Materials Lab, Pontiac, MI 48340.

Manuscript submitted September 19, 2016.

Article published online February 27, 2017

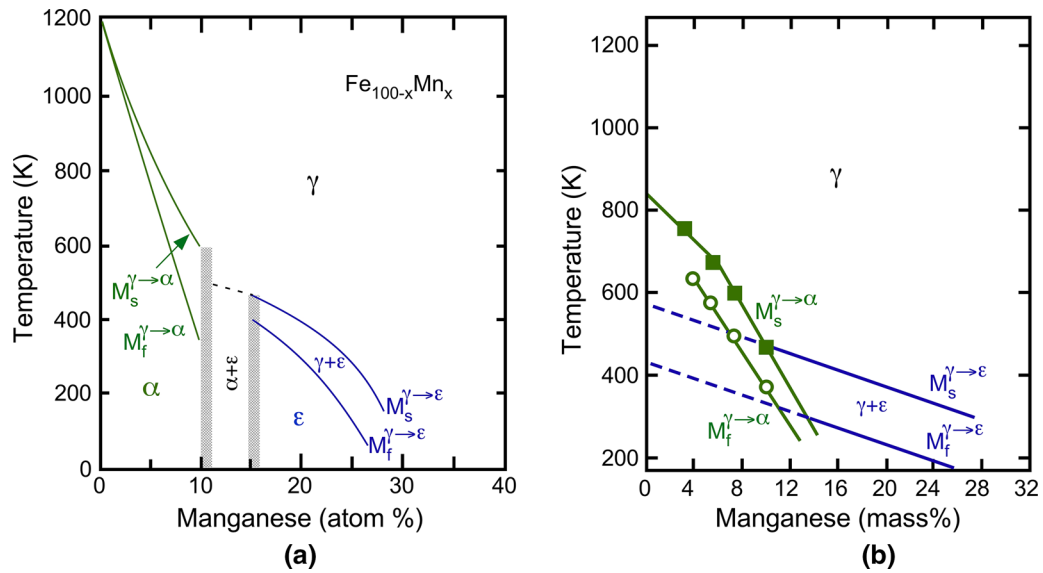


Fig. 1—(a) Phase transitions for binary Fe-Mn alloys as reported in Ref. [10]. Two martensitic reactions are shown in the range of 10 to 15 at pct Mn. Adapted from Fig. 4 from Ref. [10]. (b) Phase transitions reported by Holden *et al.*^[11] for medium Fe-Mn alloys with C ranging from 0.01 to 0.038 wt pct and Si ranging from 0.03 to 0.34 wt pct. Below 12 wt pct Mn, α -martensite was the dominant transformation product, and a mixture of ϵ and α martensite occurred between 12 and 15 wt pct Mn. Schematic drawing is based upon Fig. 1 from Ref. [11].

steels, only cobalt and aluminum additions increase the α -martensite start temperature

$$M_S(K) = 812 - 423[\text{wt pct C}] - 30.4[\text{wt pct Mn}] - 7.5[\text{wt pct Si}] + 30[\text{wt pct Al}], \quad [1]$$

$$M_S(K) = 812 - 308[\text{wt pct C}] - 30.4[\text{wt pct Mn}] - 59.9[\text{wt pct P}] - 16.6[\text{wt pct Si}] + 43.6[\text{wt pct Al}]. \quad [2]$$

$$M_S(K) = 772 - 308[\text{wt pct C}] - 32.4[\text{wt pct Mn}] - 27[\text{wt pct Cr}] - 16.2[\text{wt pct Ni}] - 10.8[\text{Si} + \text{Mo} + \text{W}] + 10[\text{wt pct Co}] \quad [3]$$

Literature reports multiple attempts to correlate the M_s to thermodynamic driving forces.^[15–19] Pisarik and Van Aken^[18] have used a modified regular solution model and the Olson and Cohen^[20,21] formulation for stacking fault energy to predict the M_s temperature for ϵ -martensite. Olson and Cohen presented a general formulation for the stacking fault energy according to Eq. [4].

$$\text{SFE (mJ/m}^2\text{)} = n\rho\left(\Delta G_{\text{Chem}}^{i \rightarrow j} + \Delta G_{\text{Str}}^{i \rightarrow j}\right) + 2\sigma^{i/j}, \quad [4]$$

where n is the number of atomic planes in the fault within the parent γ -austenite; ρ is the planar atomic density of the $\{111\}_{\gamma}$ for the steel composition using Vegard's law; and $\sigma^{i/j}$ is the interfacial energy between the parent and product phases. Literature pertaining to the development of second generation AHSS report an intrinsic stacking fault energy at room temperature

using Eq. [4] with $n = 2$.^[21,22] In the transformation of γ -austenite to ϵ -martensite, Pisarik and Van Aken^[22] determined an ϵ -martensite start temperature when the stacking fault energy becomes less than or equal to zero, and spontaneous separation of the $1/6\langle 112 \rangle$ partials occur to expand the stacking faults. A value of n was found by calculating the chemical driving force using the regular solution model and finding the temperature where the chemical driving force produced a SFE equal to zero. In this formulation, the strain energy of the transformation ($\Delta G_{\text{str}}^{\gamma \rightarrow \epsilon}$) was neglected, since as reported by Olson and Cohen, $\Delta G_{\text{str}}^{\gamma \rightarrow \epsilon}$ is less than 0.1 pct of the measured fault energy.^[21] It is interesting to point out that a value of $n = 4$ was found by Pisarik and Van Aken^[22] to best fit the experimental results of annealed medium manganese steel, in agreement with the prediction from the seminal work by Olson and Cohen^[21] for the critical size of an ϵ -martensite nucleus. Also of interest was that Pisarik and Van Aken reported that manganese had a complex relationship to the ϵ -martensite start temperature with a maximum temperature near 12 wt pct manganese, which is supported by the first principles work of Medvedeva *et al.* showing a minimum in the intrinsic stacking fault energy in the same chemical range.^[12]

In the following discussion, the α designation is ascribed to the martensitic phase and is assumed to be cubic, and thus, the thermodynamic relations for body-centered cubic iron are substituted for α -martensite. For the γ -austenite to α -martensite transformation, the interfacial energy, $\sigma^{\gamma/\alpha}$, is reported to be less than 0.2 mJ/m^2 .^[21] In contrast to the $\gamma \rightarrow \epsilon$ martensitic reaction, the $\Delta G_{\text{str}}^{\gamma \rightarrow \alpha}$ is considered to be of greater importance due to the increased volume strains associated with the $\gamma \rightarrow \alpha$ transformation. Olson and

Cohen^[20] calculated the average critical embryo size as having an $n = 13.5$ for the spontaneous α -martensite formation of an Fe-30Ni alloy, which was again the condition where according to Eq. [4] the SFE of the martensite embryo goes to zero. Grujicic *et al.*^[23] calculated the interface mobility of the α -martensite utilizing dislocation dynamics and utilized an embryo size of $n = 18$. Due to the low interfacial energy and the large defect size, the controlling terms of the SFE equation for the fcc to bcc transformation are the chemical driving force for transformation, $\Delta G_{\text{Chem}}^{\gamma \rightarrow \alpha}$, and the strain energy, which resists transformation, $\Delta G_{\text{str}}^{\gamma \rightarrow \alpha}$. In this presentation, the calculated $\Delta G_{\text{Chem}}^{\gamma \rightarrow \alpha}$ determined at the M_S^z temperature will be designated as $\Delta G_M^{\gamma \rightarrow \alpha}$ and represents the energy required to promote the martensitic reaction. The temperature at which $\Delta G_{\text{Chem}}^{\gamma \rightarrow \alpha} = 0$ is designated as T_0 , as proposed by Kaufman and Cohen.^[24] Thus, at the M_S^z temperature, it is assumed $\Delta G_M^{\gamma \rightarrow \alpha}$ is the required energy to overcome the strain of transformation, $\Delta G_{\text{str}}^{\gamma \rightarrow \alpha}$.

There have been many thermodynamic works^[15–19] to relate $\Delta G_M^{\gamma \rightarrow \alpha}$ to the M_S^z . Raghavan and Anita^[16] investigated this relationship for 1152 low-alloy steels. A linear relationship between the calculated value for the M_S^z (using the formulation based upon the work of Andrews^[17]) and the $\Delta G_M^{\gamma \rightarrow \alpha}$ was obtained resulting in $\Delta G_M^{\gamma \rightarrow \alpha}(\text{J/mol}) = 1.49M_S - 2065$. Jicheng and Zhanpeng^[15] also investigated the thermodynamic relationship between the measured M_S^z and $\Delta G_M^{\gamma \rightarrow \alpha}$ for binary Fe-C, Fe-Ni, Fe-Cr, and Fe-Cu alloys and found two different relationships that were related to martensite morphology, *i.e.*, lath *vs* plate. For lath martensite, Jicheng and Zhanpeng reported a linear relationship, similar to what Raghavan and Anita reported, for the Fe-C and Fe-Cr systems $\Delta G_M^{\gamma \rightarrow \alpha}(\text{J/mol}) = 1.23M_S - 2323$ and $\Delta G_M^{\gamma \rightarrow \alpha}(\text{J/mol}) = 2.3M_S - 3162$, respectively. For twinned martensite in the Fe-Cr and Fe-Cu systems, Jicheng and Zhanpeng observed that the $\Delta G_M^{\gamma \rightarrow \alpha}$ had a much stronger dependence upon the martensite start temperature, $\Delta G_M^{\gamma \rightarrow \alpha}(\text{J/mol}) = 11.4M_S - 5780$.^[15] These formulations for the $\Delta G_M^{\gamma \rightarrow \alpha}$ can be considered as temperature-dependent formulations for $-\Delta G_{\text{str}}^{\gamma \rightarrow \alpha} = 0$. In systems that produce an internally twinned or plate martensite, the strain energy exhibits a greater dependence upon temperature. It is often observed that the habit planes of plate martensites are of a type $\{225\}$ ^[25,26] and that these plates are internally twinned *vs* lath martensites where the variants are twin related and have habit planes $\{557\}$.^[26] Lath martensites form in packets and give the appearance of four different $\{111\}$ variants due to there only being 16 deg of separation between $\{557\}$ and $\{111\}$. In contrast, the plate morphology appears more random as individual habit plane variants appear. Therefore, it might be argued that the plate morphology segments the γ -austenite with more crystallographic variants and is internally twinned to accommodate greater strain energy at the lower transformation temperatures observed.

A. Regular Solution Model of $\gamma \rightarrow \alpha$ Martensitic Transformation

The purpose of this work was to create a thermodynamic means for formulating M_S^z based upon $\Delta G_{\text{Chem}}^{\gamma \rightarrow \alpha}$ using a regular solution model, and the work by Breedis and Kaufman is used here.^[26] This approach has been utilized by numerous authors^[22,27–30] for medium manganese steels and is formulated according to Eq. [5]

$$\Delta G_{\text{Chem}}^{\gamma \rightarrow \alpha}(\text{J/mol}) = X_{\text{Fe}}\Delta G_{\text{Fe}}^{\gamma \rightarrow \alpha} + \sum X_i\Delta G_i^{\gamma \rightarrow \alpha} + \sum X_{\text{Fe}}X_i\Delta\Omega_{\text{Fe}(i)}^{\gamma \rightarrow \alpha}, \quad [5]$$

where X_i is the atomic fraction of the solute element i . The summation accounts for all alloying elements in the system, which for this investigation are C, Mn, Si, Al, Cr, and Ni. The various alloying elements alter the free energy change for the $\gamma \rightarrow \alpha$ transformation by an amount expressed as $\Delta G_i^{\gamma \rightarrow \alpha}$. The interaction parameter in the iron-based system for solid solution expressed by $\Delta\Omega_{\text{Fe}(i)}^{\gamma \rightarrow \alpha}$. Both $\Delta G_i^{\gamma \rightarrow \alpha}$ and $\Delta\Omega_{\text{Fe}(i)}^{\gamma \rightarrow \alpha}$ were obtained from the CALPHAD reviews by Kaufman.^[31–34] The Scientific Group Thermodata Europe (SGTE)^[35] data were also reviewed and found to be the most relevant to the systems being investigated in this work. Appendix A summarizes the literature data used for both the $\Delta G_i^{\gamma \rightarrow \alpha}$ and $\Delta\Omega_{\text{Fe}(i)}^{\gamma \rightarrow \alpha}$. Nitrogen is not accounted for in the proposed model since there is no accepted interaction parameter reported in literature and represents a potential shortcoming of the model being proposed.

B. Experimental Procedure

In addition to alloys selected from the literature, nine medium manganese steels were produced by induction melting of induction iron, ferrosilicon, electrolytic manganese, pure aluminum, and carbon in the form of graphite. An argon cover gas was used to shield the melt. Calcium wire additions were made to modify oxide inclusions and remove sulfur. The molten steel was tapped from the furnace into a ladle modified with a ceramic dam to force liquid from below the surface to form the pouring stream in a manner similar to a teapot. Steels were cast with a 150 K (150 C°) superheat into phenolic urethane no-bake sand molds to form a Y-block with dimensions measuring $12.6 \times 6 \times 1.7 \text{ cm}^3$. A Foseco KALPUR® insulated riser with a diameter of 13.5 cm and height of 15.3 cm was utilized to ensure the soundness of the Y-block castings. The castings were normalized by heating to 1373 K (1100 °C), holding at temperature for 2 hours, and air cooled to room temperature, nominally 298 K (25 °C). Castings were milled to an orthogonal prism of dimensions $15.5 \times 125 \times 50 \text{ mm}^3$ and hot rolled by sequentially heating to 1223 K (950 °C), rolling, and reheating to 1223 K (950 °C). The repeated process of rolling and reheating was used to obtain the desired hot band gage of 2.5 mm and represents a total hot reduction of $87.2 \pm 6.8 \text{ pct}$. After the final roll pass, the strip was

Table I. Composition of the Produced Steels Investigated

Designation	Composition (Wt Percent)						
	C	Si	Mn	Al	N	Cr	Ni
15.1Mn	0.08	1.95	15.1	1.4	0.017		
14.3Mn	0.16	2.97	14.3	0.89	0.022		
14.2Mn	0.06	1.85	14.2	2.38	0.019		
13.9Mn	0.09	2.07	13.9	2.01	0.012		
13.0Mn	0.10	1.57	13.0	0.45	0.045		
12.5Mn	0.17	2.95	12.5	1.09	0.023		
11.5Mn	0.11	2.46	11.5	0.38	0.029		
8.1Mn	0.25	2.66	8.1	2.38	0.007		
7.9Mn	0.18	3.09	7.9	0.65	0.024		
7Mn1Ni	0.08	2.16	7.82	2.01	0.004	0.039	0.93
7Mn2Ni	0.08	2.16	7.87	2.44	0.003	0.039	1.29
7Mn3Cr	0.20	2.15	7.73	2.27	0.005	3.02	1.23

reheated to 1223 K (950 °C) for 5 minutes before being water quenched to 298 K (25 °C). Reheating was performed to obtain a recrystallized and low defect crystal structure prior to water quenching. Alloys designated as 7Mn1Ni, 7Mn2Ni, and 7Mn3Cr were produced at US Steel Research by vacuum induction melting and ingot casting. The 75-mm-thick ingots were reheated to 1533 K (1260 °C), rough hot rolled to 25-mm thickness, and air cooled to room temperature. After sectioning, the materials were reheated to 1533 K (1260 °C) and finish hot rolled to 4.6-mm thickness with simulated finishing and coiling temperatures of 1198 K and 873 K (925 °C and 600 °C), respectively. The reported chemical analysis was obtained by ion coupled plasma spectrometry after sample dissolution in hydrochloric and nitric acid. Carbon and Nitrogen contents were determined using a LECO CS6000 and a LECO TC500, respectively (Table I).

Samples for dilatometry were cut from the hot band strip with dimensions of $2.20 \times 2.45 \times 9.71 \text{ mm}^3$ with the long axis parallel to the rolling direction. Dilatometry was performed using a Lenseis L78 RITA Quenching Dilatometer at AK Steel Dearborn Works. Samples were heated to 1273 K (1000 °C) at a heating rate of 10 K/s and then cooled to room temperature at varying rates of 10, 50, and 100 K/s.

Tensile bars were milled from the hot band strip according to ASTM E8^[36] using a gage length of 50 mm and width of 12.5 mm. Tensile tests were conducted at room temperature with the tensile axis parallel to the rolling direction. Tests were performed in displacement control at a rate of 0.01 mm/s using a 245 kN servo-hydraulic test frame. Strain data were measured with a clip-on extensometer and used to determine the yield strength and modulus of elasticity.

X-ray diffraction (XRD) was performed on samples taken from the hot-rolled strip after water quenching for phase identification. XRD samples were mechanically polished to 0.1 μm using diamond paste in the longitudinal-transverse plane (polished surface parallel to the rolling plane). Diffraction patterns were obtained with a Phillips X-pert diffractometer using a flat graphite monochromator, and a Ni filter for a Cu radiation source. Phase quantifications were calculated utilizing

the Rietveld refinement described by Martin *et al.*^[37] and adjusted for the compositions investigated. Specimens for electron back-scattered diffraction (EBSD) were mechanically polished with a 0.02 μm colloidal silica solution using a vibratory polisher and examined in longitudinal-short plane (perpendicular to both the rolling plane normal and the rolling direction). Orientation image mapping *via* pattern analysis was performed on a Helios NanoLab 600 using a Nordlys detector and the AZTEC software package. The electron beam was operated at an accelerating voltage of 20.0 kV and an emission current of 5.5 nA with a 0.20 μm step size during mapping. Orientation image maps and diffraction patterns were tilt corrected for the system geometry.

II. RESULTS

Martensite start temperature, M_S^z , as determined by dilatometry, modulus of elasticity, calculated T_0 , SFE for the $\gamma \rightarrow \epsilon$ transformation at room temperature using $n = 2$, and $\Delta G_M^{\gamma \rightarrow \alpha}$ for the twelve medium manganese steels produced for this study are shown in Table II.

Formulation of the chemical-dependent Young's modulus of elasticity was derived using a combination of data from the work of Speich *et al.*,^[13] and experimental data from this investigation utilizing a least squares fit. This is shown in greater detail in the Appendix. Young's modulus was calculated according to Eq. [6] where x_i is in weight percent.

$$E(\text{GPa}) = 208.2 - 35.4x_C - 7.3x_{\text{Si}} - 1.0x_{\text{Mn}} + 3.2x_{\text{Al}} + 0.64x_{\text{Cr}} - 2.0x_{\text{Ni}} - 35.1x_{\text{N}}. \quad [6]$$

Thirty additional alloys from literature^[10,38–43] were also incorporated into the analysis and the reported values for the M_S^z , calculated Young's modulus using Eq. [6], and the $\Delta G_M^{\gamma \rightarrow \alpha}$ are included in the Appendix. A plot of $-\Delta G_M^{\gamma \rightarrow \alpha}$ vs M_S^z is shown in Figure 2 where it was found that separating the data into two populations was required to resolve the data into distinct trend lines.

Table II. Composition and Measured Modulus, Calculated Stacking Fault Energy for $n = 2$, T_0 , Martensite Start, and Driving Force for Transformation at the M_S

Designation	Measured Values				
	Modulus (GPa)	SFE (mJ/m ²)	T_0 [K (°C)] $\gamma \leftrightarrow \alpha$	M_S [K (°C)] $\gamma \rightarrow \alpha, \alpha + \varepsilon$	$\Delta G_M^{\gamma \rightarrow \alpha}$ (J/mol)
15.1Mn	153	7.9	624 (351)	414 (141)	-1076
14.3Mn	147	5.0	609 (336)	417 (144)	-943
14.2Mn	144	16.1	667 (394)	390 (117)	-1310
13.9Mn	169	13.3	657 (384)	352 (79)	-1489
13.0Mn	168	-2.2	671 (398)	335 (62)	-1811
12.5Mn	160	6.8	655 (382)	355 (82)	-1606
11.5Mn	181	-1.8	701 (428)	409 (136)	-1575
8.1Mn	182	23.5	762 (489)	429 (156)	-1707
7.9Mn	173	6.2	767 (494)	458 (185)	-1716
7Mn1Ni	186	20.2	818 (545)	505 (232)	-1740
7Mn2Ni	211	25.6	823 (550)	473 (200)	-1549
7Mn3Cr	166	26.9	726 (453)	361 (88)	-1785

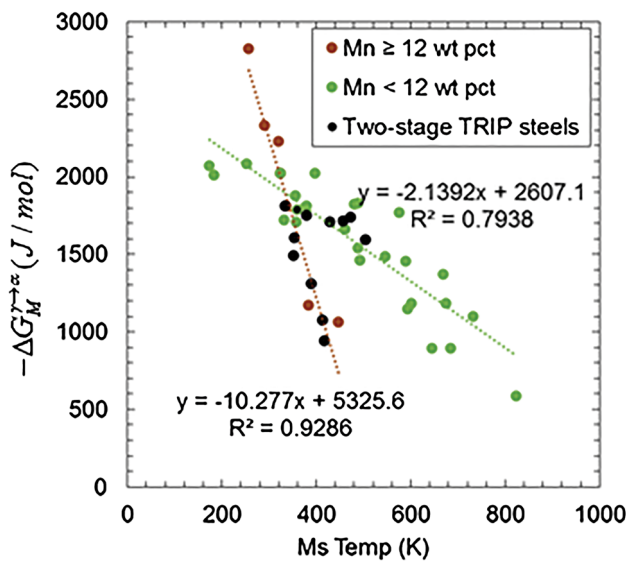


Fig. 2—Plot of the $-\Delta G_M^{\gamma \rightarrow \alpha}$ as a function of M_S temperature. Two distinct relationships can be found between the martensite start and the driving force for transformation at the martensite start temperature based on the Mn content in the steels. The two-stage TRIP steels are shown in black (Color figure online).

Alloys containing less than 12 wt pct Mn produced a behavior similar to what Raghavan and Anita reported,^[16] and what Jicheng and Zhanpeng^[15] proposed for microstructures containing lath martensite. Greater temperature dependence is observed for alloys containing greater than 12 wt pct Mn and is similar to what Jicheng and Zhanpeng^[15] proposed for plate martensite structures.

A. Incorporation of Young's Modulus and Application of SFE model to Calculate M_S^z

The strain energy of transformation is expected to be a function of the moduli of both parent and product phases. For steel, the difference in modulus between γ -austenite and α -martensite is expected to be small as

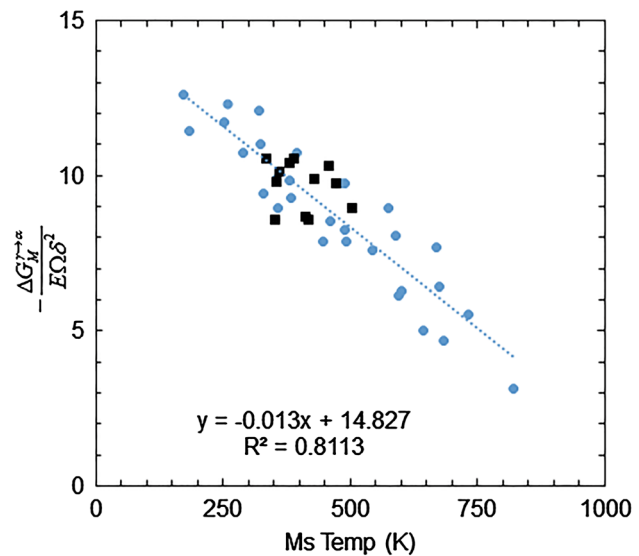


Fig. 3—The relationship between the $\Delta G_M^{\gamma \rightarrow \alpha}$ normalized to the modulus of elasticity (E), molar volume (Ω), and lattice misfit (δ) as a function of the M_S^z with two-stage TRIP steels are shown as black squares (Color figure online).

reported by Ghosh and Olson,^[44] and both γ -austenite and α -martensite would have similar dependence upon composition. The strain energy would also be dependent upon the transformation temperature and increase as the M_S^z temperature decreased. A plot of $-\frac{\Delta G_M^{\gamma \rightarrow \alpha}}{E\Omega\delta^2}$ vs the M_S^z is shown in Figure 3, where E is the modulus calculated according to Eq. [6], using units of Pa, Ω is the molar volume calculated for iron 7.15×10^{-6} (m³/mol), δ is the lattice misfit between the γ -austenite and α -martensite with an approximate strain value of 1.11×10^{-2} (m/m), and T is the temperature in Kelvin. A single trend line was used to represent both data sets with the compositional limits for the data shown in Table III.

A temperature and composition-dependent strain energy relationship was derived from Figure 3 that must be overcome to form the α -martensite within the

Table III. Compositional Limits in Weight Percent for the 42 Alloys Found in Literature and Produced Used for the Model Development with 173 K (−100 °C) < M_S^z < 822 K (549 °C) [average 450 K (177 °C)]

	C	Si	Mn	Al	N	Cr	Ni
Min	0	0	0	0	0	0	0
Max	0.3	3.09	15.7	2.44	0.614	17	15.1
Ave	0.08	1.8	8.2	1.3	0.126	8.9	5.8

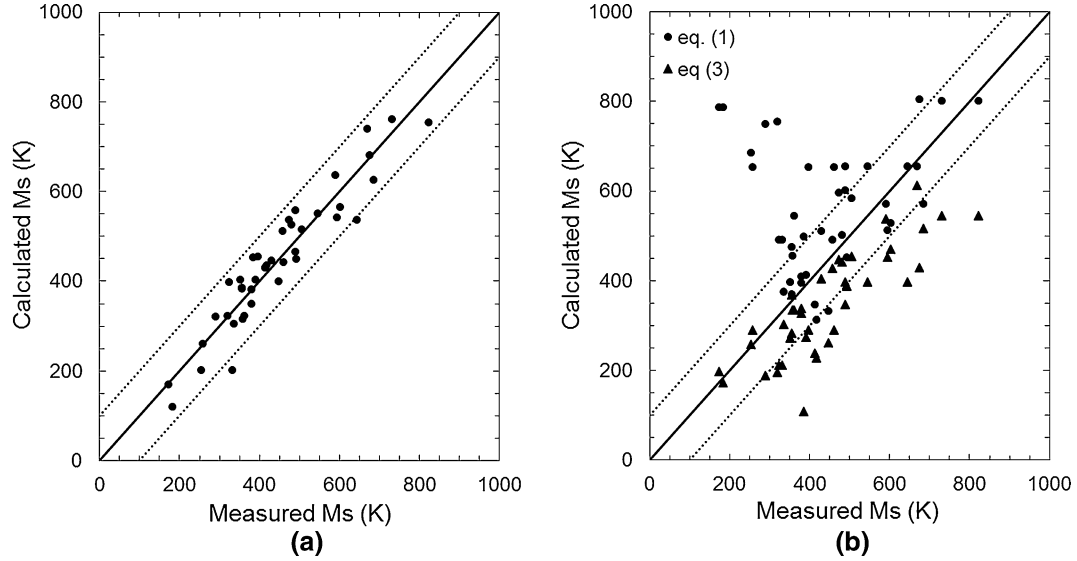


Fig. 4—(a) Correlation between the measured M_S^z and calculated for the proposed strain model compared to (b) two empirical models from DeCooman and Speer^[14] for the same alloys shown in (a). Equation [1] shows a poor fit to the data since many of the alloys used in the plot contain Ni and Cr. In a similar fashion, alloys containing aluminum fall below the identity line since the temperature increase associated with aluminum is not included in Eq. [3].

parent γ -austenite, and this relationship is given in Eq. [7]

$$\Delta G_{\text{Str}}^{\gamma \rightarrow \alpha} (\text{J/mol}) = E\Omega\delta^2(14.8 - 0.013T). \quad [7]$$

The temperature at which the sum of $\Delta G_{\text{Chem}}^{\gamma \rightarrow \alpha}$ and $\Delta G_{\text{Str}}^{\gamma \rightarrow \alpha}$ is zero is the point at which the stacking fault energy of the martensitic embryo is zero, and there is no restrictive force acting on the $\frac{a}{2}\langle 1\bar{1}0 \rangle_{\gamma}$ dislocation to separate as partials. A comparison of the calculated vs measured M_S^z for the 42 investigated alloys is shown in Figure 4(a), and a scatter band of ± 100 K (100 C°) is shown for reference. For comparison, two different empirical models, Eqs. [1] and [3] are shown in Figure 4(b) for the same alloys.

III. DISCUSSION

This study shows that the inclusion of a compositionally dependent Young's modulus, as included in the strain energy of transformation, has the ability to predict a martensite start temperature independent of martensite morphology. As done in previous studies, a regular thermodynamic solution model was used to determine the driving force for transformation at the

measured martensite start temperature and was related to the strain energy that must be overcome during transformation. While this approach of showing $\Delta G_M^{\gamma \rightarrow \alpha}$ as a function of temperature has been used by other authors in previous works,^[23,45,46] the work presented here has shown that a single relationship for both lath and plate martensite can be produced by considering a compositional-dependent Young's modulus. Highly alloyed steels in the present study have a low Young's modulus and, according to the proposed model, a lower strain energy. Thus, the required chemical driving force to overcome the strain energy of transformation is lower, and this translates into a smaller undercooling below T_0 and a higher M_S temperature.

For manganese contents greater than 12 wt pct, the temperature-dependent term shown in Figure 2 is within 2 pct of what Jicheng and Zhanpeng^[15] showed for plate martensites that are internally twinned. Athermal α -martensite reported by Pisarik and Van Aken^[47] for the 14.3 Mn alloy is shown to be plate-like when nucleated within the ε -martensite and the plate variants are twin related. Further work to classify the internal structure of the martensites will be a topic of a future study. However, Holden *et al.* reported that α -martensite plates were not internally twinned when nucleated within the ε -martensite, and the internal structure was the result of slip.^[11]

The model proposed here covers a wide range of compositions and can be applicable to even low-alloy steels reported by Atkins.^[48] However, due to the broad range of alloys and temperatures, the scatter found in Figure 4(a) of ± 100 K (100 C°) is larger than desired. Inclusion of a compositional dependence for the molar volume and a temperature dependence for the unconstrained misfit is expected to decrease the uncertainty, but adds considerable complexity to the model.

Ghosh and Olson^[46] attempted a similar thermodynamic approach to the martensite start of 41 alloys incorporating a chemical and temperature-dependent term, which investigated both dilute- and solute-rich binary alloys but ignored magnetic interactions. They proposed a compositional-dependent term based on the interfacial frictional work of the martensitic interface according to Eq. [8] with a separate term for cobalt (Co)

$$W_{\mu} = \sqrt{\sum_i (K_{\mu}^i X_i^{0.5})^2} + \sqrt{\sum_j (K_{\mu}^j X_i^{0.5})^2} + \sqrt{\sum_k (K_{\mu}^k X_i^{0.5})^2} + K_{\mu}^{\text{Co}} X_{\text{Co}}^{0.5}, \quad [8]$$

where K_{μ} is the athermal strength of different solutes and $i = \text{C, N}$; $j = \text{Cr, Mn, Mo, Nb, Si, Ti, V}$; and $k = \text{Al, Cu, Ni, W}$, which were experimentally determined according to the flow stress for slip deformation of single crystals as a function of composition. Ghosh and Olson theorized that each solute atom acted as obstacles for slip deformation, similarly to what Grujicic *et al.*^[23] assumed with respect to point defects. Ghosh and Olson concluded that the solute atoms acted as barriers to the mobility of the martensitic interface with little differentiation between solute types.^[46] However, both studies assumed that chemical and electronic interactions and the modulus were incorporated in the measured athermal strength. Ghosh and Olson noted that their work was based only on binary systems ranging from the dilute to highly concentrated, but felt their results might not be globally applicable to multicomponent systems.^[46] In contrast to prior work, the work presented here was an attempt to look at a multicomponent approach using the Young's modulus.

Surprisingly, Al is found to have a positive effect on the modulus in Eq. [6], and this appears to relate to an increase in the M_{S}^{α} . Work by Takeuchi^[45] found that aluminum had a negative effect on the shear modulus; however, the works by both Takeuchi^[45] and Speich *et al.*^[43] investigated binary systems solely. The works of both Takeuchi and Speich stated that these effects are potentially not additive to the modulus in multicomponent systems. Interstitial carbon and nitrogen have the strongest negative impact on the Young's modulus as shown in Eq. [6]. It should be noted that addition of aluminum is expected to increase the AlN solvus temperature and reduce the amount of nitrogen in solid solution by the precipitation of AlN. Thus, the positive increase in modulus resulting from aluminum addition may be interpreted as nitrogen mitigation, and as a result, aluminum is observed as a positive contributor to the Young's modulus in the work presented here.

Table IV. Volume Percent Phases of Seven Two-Stage TRIP Steels Presented in the Current Work and the Five Alloys from Literature

Designation	Volume Percent Phase from XRD		
	γ	ε	α
15.1Mn	26.1	32.4	41.2
14.3Mn	27.6	46.5	25.9
14.2Mn	68.3	3.7	28
13.9Mn	41.1	27.2	31.8
13.0Mn	1.0	60.2	38.8
12.5Mn	12	83	5
11.5Mn	5.7	24.8	69.5
49	93	7	0
50	72.6	27.4	0
50	69.1	30.9	0
50	48.8	51.2	0
50	91.8	8.2	0

Utilizing the results of Pisarik and Van Aken^[22] and the results presented here M_{S}^{α} and $M_{\text{S}}^{\varepsilon}$ can be calculated and compared to the microstructural constituents of the seven two-stage TRIP alloys (reported in Table IV) containing ε -martensite in the starting microstructure. Each alloy was reheated to a fully austenitic state and water quenched. In addition, a two-stage TRIP steel reported by Yang *et al.*^[49] and four alloys from Kim *et al.*^[50] were also considered. A comparison of the reported phase fractions from these studies show that the volume percent retained γ -austenite is related to the difference between the $M_{\text{S}}^{\varepsilon}$ and M_{S}^{α} as shown in Figure 5, which hopefully demonstrates the utility of the proposed methodology for predicting start temperatures. These results also suggest that an initial transformation to ε -martensite ($M_{\text{S}}^{\varepsilon} > M_{\text{S}}^{\alpha}$) should be nearly complete with room temperature retained γ -austenite less than 10 vol pct. Formation of ε -martensite would then reduce the chemical driving force and lower the α -martensite start temperature. It should be noted that the start temperature for ε -martensite was determined using $n = 4$ in Eq. [4]. Larger values of n would cause the ε -martensite to form at even higher temperatures. This may suggest that retention of γ -austenite is dependent upon nucleating α -martensite and removing the chemical driving force for potential ε -martensite embryos.

It is now possible using the work of Pisarik and Van Aken^[22] and the work presented here to predict the effect of alloying elements in the medium-Mn steel. Plots of $\Delta G_{\text{Chem}}^{\varepsilon \rightarrow \alpha}$ at room temperature, the $M_{\text{S}}^{\varepsilon}$ temperature, the M_{S}^{α} temperature, and the difference between the $M_{\text{S}}^{\varepsilon}$ and M_{S}^{α} are shown in Figure 6 with respect to Mn, Si, and Al content with C and N fixed at 0.07 and 0.017 wt pct as previously done in Reference 22. Upon review of Figure 6(a), it is observed that the ε -martensite becomes more stable relative to α -martensite by increasing Mn. Increases in either Si or Al decrease the stability of ε -martensite, and these results appear to be in good agreement with the reported first principles work of Limmer *et al.*^[51] showing that Al and Si increase the

intrinsic stacking fault energy. This is corroborated by Yang *et al.*,^[49] for an alloy that contained 0.24C-0.15Si-21.5Mn-balFe (wt pct), and shows a duplex γ -austenite and ε -martensite microstructure. From Figure 6(b), a maximum in the M_S^e temperature occurs at roughly 12.5 to 13 wt pct manganese and M_S^e decreases as aluminum content increases. In Figure 6(c), the effect of manganese content on the M_S^e is shown to produce a minimum at 12.5 wt pct Mn leading to an M_S^e of about 320 K (47 °C) and the M_S^e increases in temperature as aluminum is increase from 0.5 to 2.5 wt pct. The minima in M_S^e narrows in manganese composition and shifts slightly to a lower manganese content of 12.25 wt pct as aluminum content increased. Medvedeva *et al.*^[18] calculated a minimum in the intrinsic stacking fault energy at a manganese concentration of 12 at. pct, equivalent to 12.2 wt pct Mn, and this minima appears to be expressed in the thermodynamic model proposed by Pisarik and Van

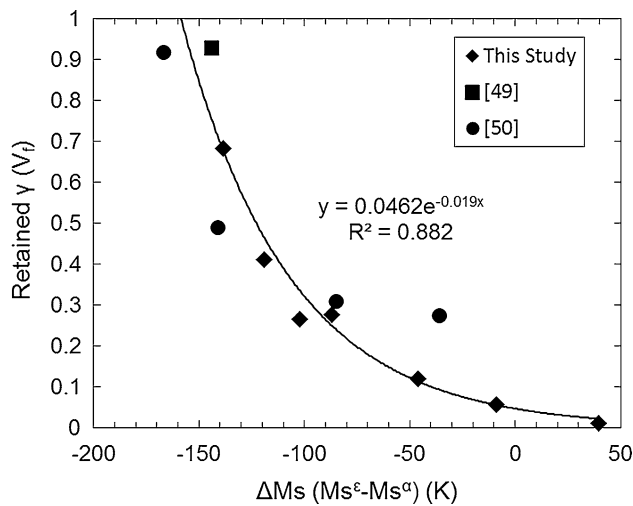


Fig. 5—Relationship between the retained γ -austenite and the difference between the start temperatures of the ε - and α -martensites. The relationship shows similarity to a Koistinen–Marburger type relationship.

Aken^[22] for a maximum in M_S^e , and the current model for a minimum in the M_S^e at 12.5 wt pct Mn. Aluminum appears to increase the M_S^e as reported by most empirical models, as observed in Figure 6(c), where a narrowing of the minimum of the contour map occurs as aluminum is increased. This is assumed to be an effect of increasing the intrinsic stacking fault energy and a reduced N content in solution as nitrogen is known to depress the M_S^e . Removal of nitrogen from solid solution would also increase the intrinsic stacking fault energy in the steel, since nitrogen has been shown by first principle calculations to decrease the intrinsic stacking fault energy.^[52–54]

At manganese concentrations greater than 15 at pct, Acet *et al.*^[10] noted that α -martensite was no longer observed upon quenching as shown in Figure 1(a). This observation may be explained by the decreasing chemical driving force $\Delta G_{\text{Chem}}^{\varepsilon \rightarrow \alpha}$ as manganese is increased as shown in Figure 6(a). However, this assumes ε -martensite forms first. It is observed that in Figure 6(c) the M_S^e is increasing up to a temperature of 525 K (252 °C) at a manganese content of 19 wt pct; clearly, this result is not observed in reported literature nor in the results of this study. From this and the observed compositional range of Table III, it should be understood that the proposed model is not applicable for manganese contents greater than 15 wt pct. The extended range of manganese compositions shown in Figure 6 are presented to demonstrate the limits of the model calculations.

Figure 6(d) combines the data of both Figures 6(b) and (c) to produce a phase map prediction where M_S^e is greater than M_S^z . It can be observed that to produce an alloy that will first transform to ε -martensite and then transform to α -martensite would require a composition of 13 wt pct Mn and less than 0.5 wt pct Al. However, Pisarik and Van Aken^[47] reported that a 15.1 Mn alloy in the as-cast condition exhibited both athermal martensitic reactions. This can be explained by considering segregation during solidification. A Scheil–Gulliver segregation model in FactSage™ was used to calculate the composition of the last 15 pct by weight liquid and represents the alloy segregated region defined as “Rich”

Table V. Calculated Compositions of the Chemically Segregated Regions and Martensite Start Temperatures of the 15.1Mn, 14.3Mn, and 11.5Mn Alloys

Alloy	C	Si	Mn	Al	N	M_S^e n = 4 [K (°C)]	M_S^e n = 8 [K (°C)]	M_S^z [K (°C)]
15.1Mn								
Bulk	0.08	1.95	15.1	1.4	0.017	315 (42)	361 (88)	424 (151)
Lean*	0.05	1.66	13.9	1.1	0.007	387 (114)	390 (117)	369 (96)
Rich*	0.16	3.59	21.6	3.0	0.047	112 (–161)	140 (–133)	522 (249)
14.3 Mn								
Bulk	0.16	2.97	14.3	0.89	0.022	336 (63)	380 (107)	427 (154)
Lean	0.11	2	12.3	0.92	0.015	355 (82)	388 (115)	344 (71)
Rich	0.17	3.2	18.0	0.63	0.067	331 (58)	379 (106)	536 (263)
11.5 Mn								
Bulk	0.11	2.46	11.5	0.38	0.029	378 (105)	421 (148)	410 (137)
Lean	0.09	1.90	11.3	0.39	0.017	383 (110)	427 (154)	427 (154)
Rich	0.14	2.60	12.7	0.32	0.053	379 (106)	412 (139)	323 (50)

* denotes values which are calculated.

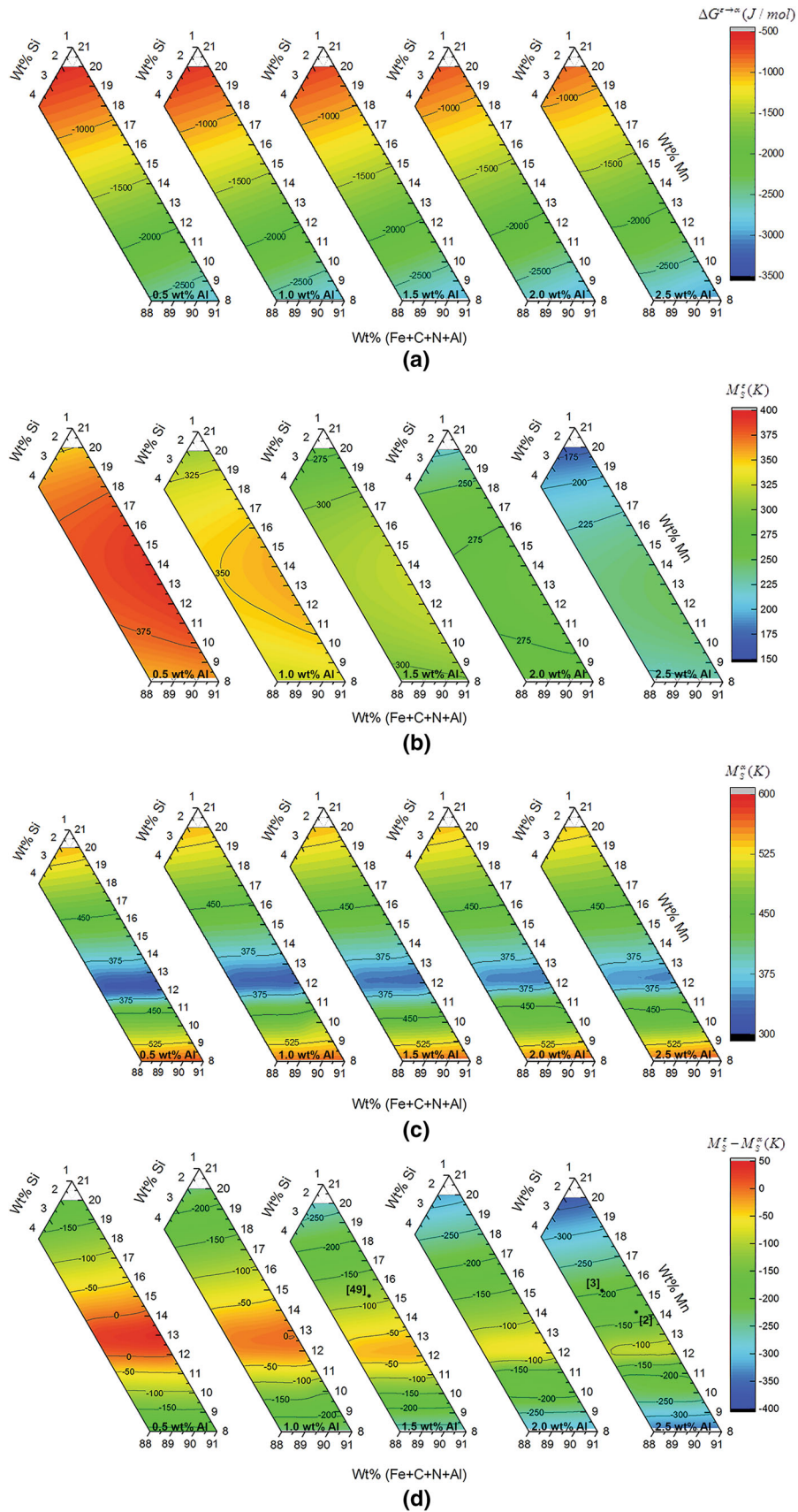


Fig. 6—Effect of composition on (a) the $\Delta G_{\text{Chem}}^{\epsilon \rightarrow \alpha}$ (b) M_S^ϵ , (c) M_S^α and (d) the difference of the start temperatures ($M_S^\epsilon - M_S^\alpha$) in the Fe, Mn Al Si system. Value of 0.07 wt pct C and 0.017 wt pct N were held constant (Color figure online).

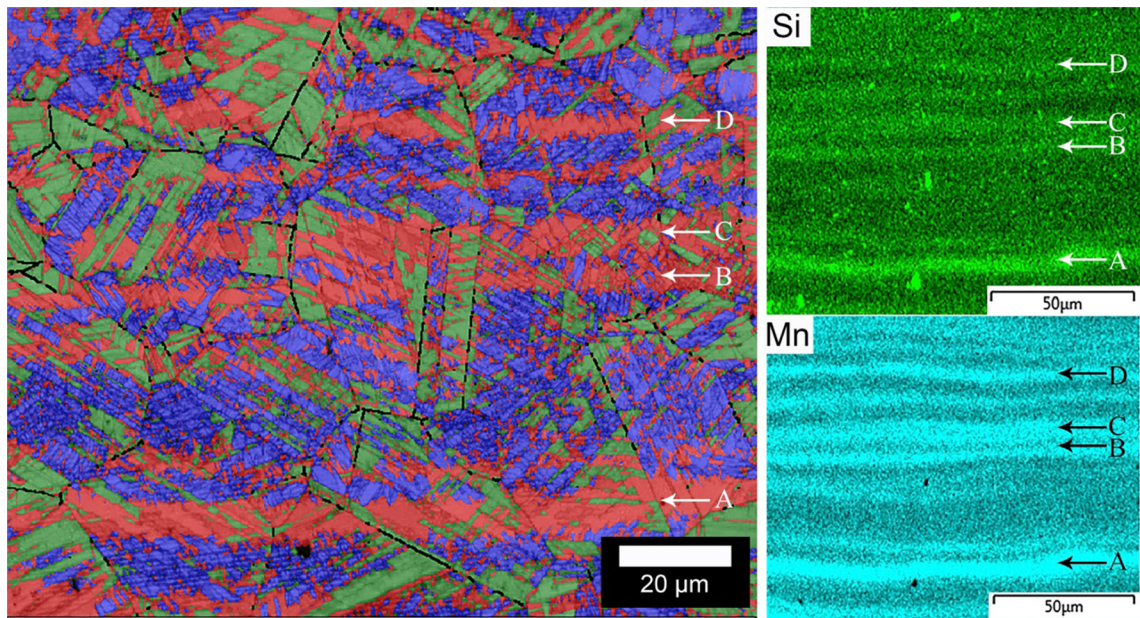


Fig. 7—An EBSD-OIM image (left) of the 14.3Mn alloy where γ -austenite is green, ϵ -martensite is red, and α -martensite is blue. An EDS map of the Si (upper right) and Mn (lower right) of the same area is shown on the right, with areas of high concentration showing greater intensity in color (Color figure online).

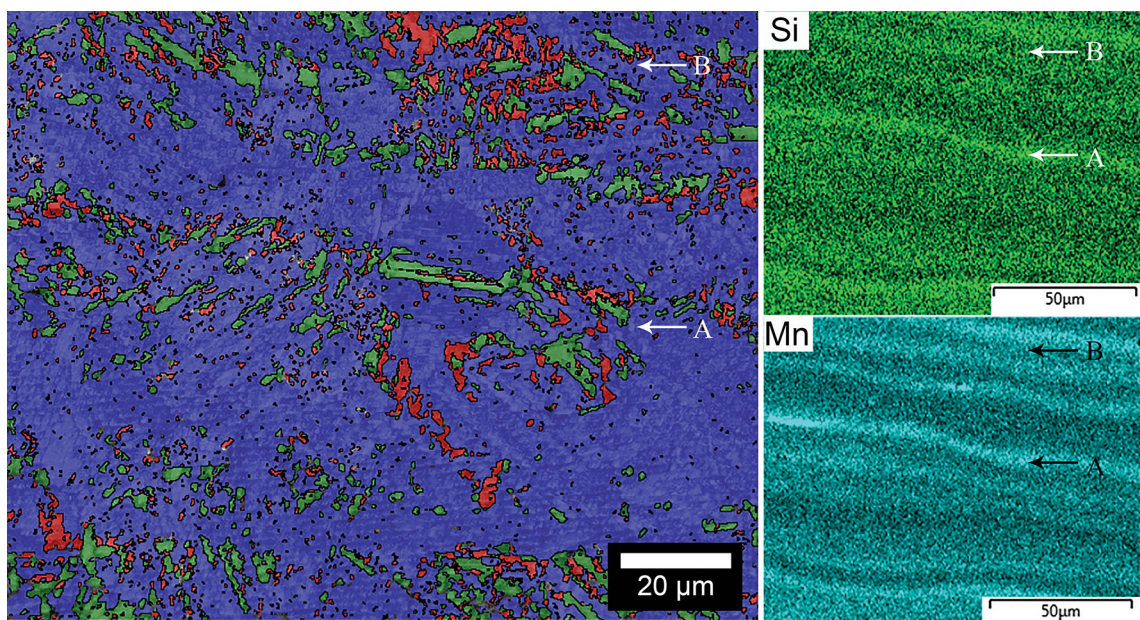


Fig. 8—An EBSD-OIM image (left) of the 11.5Mn alloy in the reheated and water-quenched condition where γ -austenite is green, ϵ -martensite is red, and α -martensite is blue. An EDS map of the Si (upper right) and Mn (lower right) of the same area is shown on the right, with areas of high concentration showing greater intensity in color (Color figure online).

in Table V. The “Lean” values reported in Table V were calculated by mass balance to yield the “Bulk” composition. It is observed that the first 85 pct (solute lean) to solidify has an average composition of 0.05C-1.660Si-13.9Mn-1.1Al-0.007N-balFe (wt pct) which leads to an $M_S^e = 387$ K (114 °C) and an $M_S^z = 369$ K (96 °C) which should lead to a two-stage athermal martensite transformation as previously shown by Pisarik and Van Aken.^[47]

A similar result can be shown for the 14.3Mn alloy presented here, and a combined EBSD-OIM/EDS map is shown in Figure 7. The EDS mapping of Mn and Si show bands of high and low concentration parallel to the rolling direction. Solute-rich regions are marked with arrows, and these bands are denoted by letters on both the EDS and EBSD-OIM maps. The solute-rich regions are primarily comprised γ -austenite and ϵ -martensite, which is in agreement with the expected

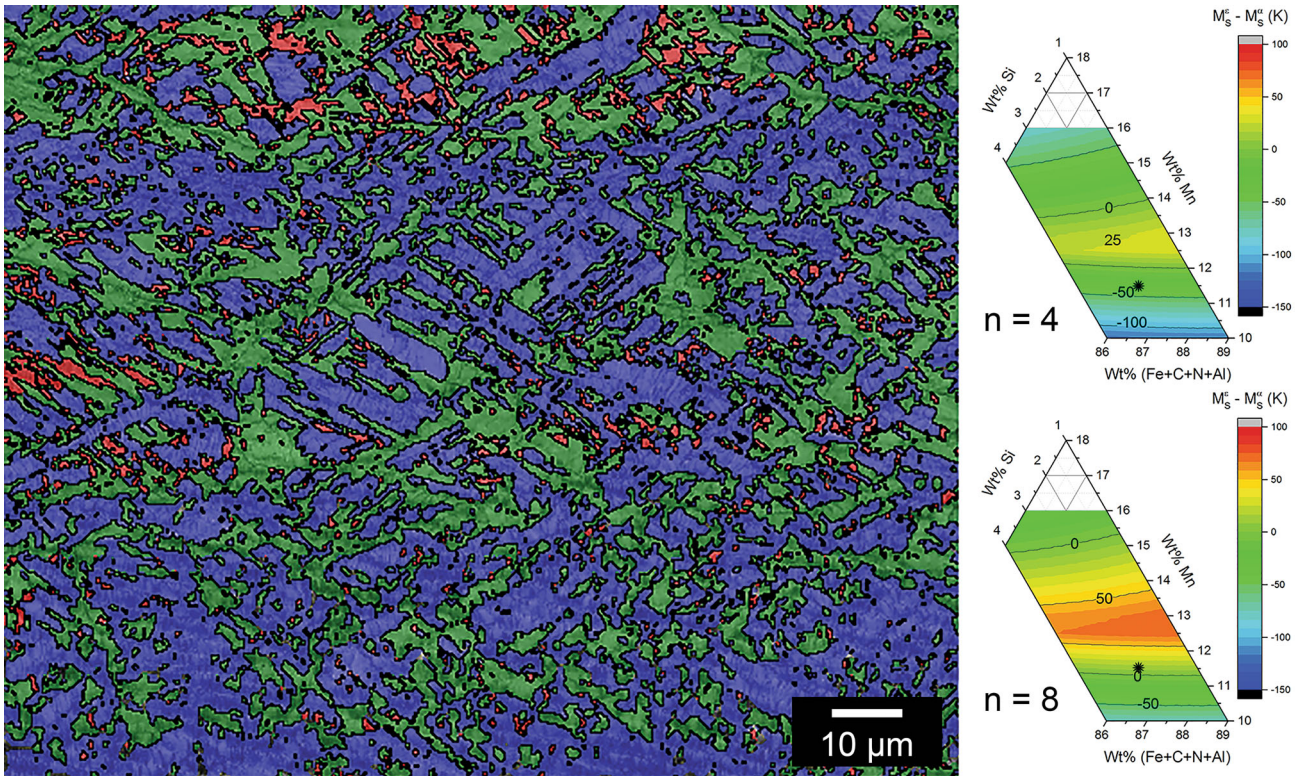


Fig. 9—EBSD-OIM image (left) of the 11.5Mn alloy in the air cooled condition where γ -austenite is green, ϵ -martensite is red, and α -martensite is blue. The $M_S^z - M_S^\epsilon$ (right) is shown for a fixed 0.11 wt pct C, 0.38 wt pct Al, and 0.029 wt pct N corresponding to the 11.5Mn alloy. A nucleating defect of $n = 4$ (upper right) is used to calculate the M_S^z , and a value of $n = 8$ (lower right) to calculate the M_S^z (Color figure online).

phases in the works by both Acet *et al.*^[10] and Yang *et al.*^[49] Solute-lean regions are comprised of α -martensite, which nucleated within the ϵ -martensite and γ -austenite. As shown in Table V, the solute-lean areas are found to have a composition of 0.11C-2.00Si-12.3 Mn-0.92Al-0.015N-balFe (wt pct). This composition according to the proposed model would have an $M_S^z = 344$ K (71 °C) and an $M_S^\epsilon = 355$ K (82 °C) using an $n = 4$, for a well-annealed γ -austenite. The Mn- and Si-rich regions are dominated by ϵ -martensite as might be predicted in Figure 1. The proposed model incorrectly predicts α -martensite for these segregated regions as shown in Table V for the as-solidified microstructure. Again, this demonstrates the limitation of the proposed model to manganese compositions less than 15 wt pct. It has been shown by De Cock *et al.*^[55] that rolling direction can affect the A_{c1} and A_{c3} , which would imply a dependence of the Ms temperature upon the rolling direction. However, no discernable texture was observed in the EBSD-OIM studies reported here.

At this point, it is instructive to look at the 11.5Mn alloy, and a similar mapping of EBSD-OIM/EDS is shown in Figure 8. The segregation analysis is shown in Table V. Here the solute-rich region is predicted to have an M_S^z (for an $n = 4$) which is 379 K (106 °C) and an M_S^ϵ of 323 K (50 °C). The phase mapping shows a combination of ϵ -martensite, α -martensite, and γ -austenite, which is in reasonable agreement with the model. A predominately α -martensite microstructure is observed in the solute-lean regions, which is expected when M_S^z

[427 K (154 °C)] is greater than M_S^ϵ [383 K (110 °C)]. A consideration of $M_S^z - M_S^\epsilon$ would suggest that the solute-lean regions would contain greater γ -austenite, and the opposite is observed in Figure 8. It should be noted, however, that the values predicted from Figure 5 are calculated according to the bulk chemistry. Furthermore, the microstructures examined in Figures 7 and 8 have some degree of homogenization from thermomechanical processing and the uncertainty in the calculated M_S^z as shown in Figure 4(a) is ± 100 K (100 °C). Thus, the prediction of the microstructure appears quite reasonable if one works within the limitation of the proposed model.

Sensitivity to processing can be demonstrated using the 11.5Mn alloy. Figure 9 shows the EBSD-OIM phase mapping after the alloy had been air cooled directly after the final hot rolling pass. The exit temperature from the rolling mill was measured to be 1048 K (775 °C). The γ -austenite volume fraction was measured to be 24.3 vs 5.7 pct in the annealed and water-quenched condition as shown in Figure 8. The difference in retained γ -austenite for the reheated and water-quenched sample (Figure 8) as compared to a specimen that was air cooled directly after final rolling could be due to stresses caused during quenching. Stresses developed during rapid temperature and volume change may lead to stress induced martensite as opposed to athermal martensite. It is interesting to note that in both the air cooled and water-quenched samples, the volume percent of ϵ -martensite is the same 24 pct. It has been well

documented^[50,56] that the transformation from $\gamma \rightarrow \varepsilon$ results in a volume contraction compared to the $\gamma \rightarrow \alpha$ transformation, which is a volume expansion. Thus, the ε -martensite acts as an internal stress relief for thermal contraction and may be promoted during quenching. M_S^ε is very sensitive to nucleating defect size (n) in the SFE equation^[20,22] as well as grain size.^[57–59] The nucleating defect size of $n = 4$ assumes a well-annealed state, and this might not be appropriate for the processing performed here or in previous studies.^[2,3,9] Yang *et al.*^[56] produced the well-annealed state after 2 days of homogenization at 1473 K (1200 °C). The effect of changing the defect size for a fixed 0.11C-0.38Al-0.029N-balFe alloy with varying amounts of Mn and Si is also shown in Figure 9. If a defect size of $n = 8$ is considered for the ε -martensite, the region of $M_S^\varepsilon - M_S^\alpha > 0$ expands to a composition range of 11.4 to 15.3 wt pct Mn and a Si content greater than 1 wt pct as shown in Figure 9. Table V shows that an $n = 8$ value produces an ε -martensite start temperature 44 K (44 C°) higher than the $n = 4$ case for ε -martensite of the lean composition. The difference in martensite start temperatures becomes zero and both martensite types would be expected in the microstructure for the bulk and lean composition. If α -martensite had formed first, there would be no chemical driving force to form ε -martensite. Clearly, more work is required to understand these alloys, but the proposed model does provide explanatory power when investigating microstructure and processing relationship in these mid-manganese steels.

IV. CONCLUSION

A new composition-based method for calculating the chemical driving force of the $\gamma \rightarrow \alpha$ transformation, $\Delta G_{\text{Chem}}^{\gamma \rightarrow \alpha}$, using a regular solution model has been used to predict the strain energy necessary to overcome for the formation of α -martensite. A composition and temperature-dependent strain energy $\Delta G_{\text{str}}^{\gamma \rightarrow \alpha}$ has been proposed for the formation of α -martensite, and by setting $\Delta G_{\text{Chem}}^{\gamma \rightarrow \alpha} + \Delta G_{\text{str}}^{\gamma \rightarrow \alpha} = 0$, an M_S^α can be determined. The role of the chemical-dependent Young's modulus, lattice misfit, and molar volume is important in providing a unified expression between $\Delta G_{\text{Chem}}^{\gamma \rightarrow \alpha}$ and M_S^α for both lath and plate martensites. This model has shown good correlation between the measured start temperature for

42 different alloys with large variations in composition and start temperatures. A microstructural relation was also shown for the volume fraction retained γ -austenite and the difference between the calculated M_S^ε and M_S^α of twelve different ε -martensite containing alloys. The model has an uncertainty of ± 100 K (100 C°), but within this uncertainty, the model has explanatory power for the microstructures observed in mid-manganese steels. The model is limited in its ability to predict α -martensite to compositions less than 15 wt pct Mn. Processing history was also shown to play a role in the prediction of ε -martensite and that using a larger $n = 8$ value for the ε -martensite embryo size can provide better correlation to the observed microstructure. It might be concluded from the work presented here that if sufficient fitting parameters are used any phenomenon can be modeled. The ability to model both lath and plate martensite, however, shows that the methodology has utility and justifies further study.

ACKNOWLEDGMENTS

This work was supported by the Peaslee Steel Manufacturing Research Center (PSMRC). Companies directly involved in this work include AK Steel, ArcelorMittal, Nucor Steel, and U. S. Steel. The FEI Helios NanoLab dual beam FIB was obtained with a Major Research Instrumentation grant from the National Science Foundation under contract DMR-0723128. The authors also acknowledge the support of the Materials Research Center and in particular Dr. Clarissa Wisner, Dr. Jessica TerBush, and Dr. Eric Bohannon for guidance and training in using the FIB and performing the XRD work. The assistance from Dr. Daniel Baker while employed at AK Steel on performing dilatometry of the alloys shown in Table II is kindly acknowledged. Finally, the support from US Steel and Todd Link for casting and hot rolling the 7Mn1Ni, 7Mn2Ni, and 7Mn3Cr alloys was greatly appreciated.

APPENDIX

Alloying elements alter the Gibb's free energy change for the $\gamma \rightarrow \alpha$ transformation by $\Delta G_i^{\gamma \rightarrow \alpha}$, which is

Table AI. Equations for Free Energy and Interaction Parameter Difference Used

Free Energy Difference (J/mol) (T in K)		Interaction Parameter Difference (J/mol) (X_i in Atomic Fraction)	
Fe	$\Delta G^{\gamma \rightarrow \alpha} = 1462.4 - 8.282T + 0.64 \times 10^{-3}T^2 + 1.15T \times \ln(T)$	Fe (Fe)	—
Mn	$\Delta G^{\gamma \rightarrow \alpha} = -1477 + 0.514T - 2.74 \times 10^{-3}T^2 + 1.65 \times 10^{-6}T^3$	Fe (Mn)	$X_{\text{Fe}}(4100 + 4.69T) + X_{\text{Mn}}(5188 + 1.51T) - (16.99T - 18,870)$
Si	$\Delta G^{\gamma \rightarrow \alpha} = 4000 - 0.7T$	Fe (Si)	$7113 \times (X_{\text{Fe}} - X_{\text{Si}})$
Al	$\Delta G^{\gamma \rightarrow \alpha} = 10,083 - 4.813T$	Fe (Al)	$-7280X_{\text{Fe}} - 62,760X_{\text{Al}}$
C	$\Delta G^{\gamma \rightarrow \alpha} = 8368$	Fe (C)	$(59,412 - 34.9T) \times (X_{\text{Fe}} + X_{\text{C}})$
Cr	$\Delta G^{\gamma \rightarrow \alpha} = -7284 - 0.163T$	Fe (Cr)	$17,699 - 4.18T$
Ni	$\Delta G^{\gamma \rightarrow \alpha} = 8715.1 - 3.556T$	Fe (Ni)	$5230 - 8.37T$

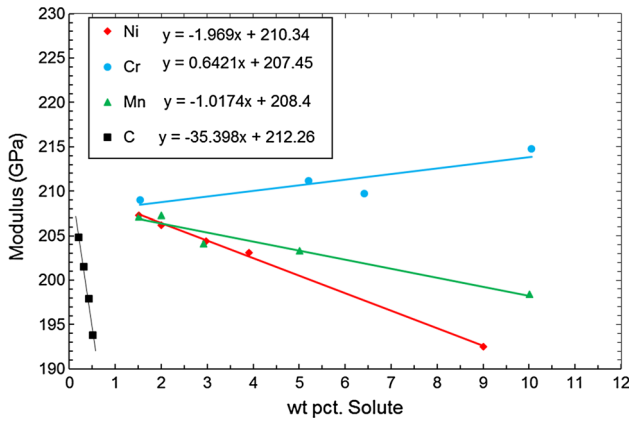


Fig. A1—Data for the effect of alloying element on the modulus of steel. Adapted from Ref. [13].

determined using Eq. [A1]. The interaction parameter in the iron-based system for a solid solution is represented as $\Delta\Omega_{\text{Fe}(i)}^{\gamma \rightarrow \alpha}$, which is calculated using Eq. [A2]. The values for the $\Delta G_i^{\gamma \rightarrow \alpha}$ and $\Delta\Omega_{\text{Fe}(i)}^{\gamma \rightarrow \alpha}$ for the alloying element, i are shown in Appendix Table AI

$$\Delta G_i^{\gamma \rightarrow \alpha} = G_i^{\alpha} - G_i^{\gamma}, \quad [\text{A1}]$$

$$\Delta\Omega_{\text{Fe}(i)}^{\gamma \rightarrow \alpha} = \Omega_{\text{Fe}(i)}^{\alpha} - \Omega_{\text{Fe}(i)}^{\gamma}. \quad [\text{A2}]$$

To calculate the modulus, data from Speich *et al.*[13] was used for C, Mn, Cr, and Ni from the data in Figure A1. To determine the effect of Si, Al, and N, the modulus is calculated for the known alloys in Appendix Table AII with elements Ni, Cr, Mn, and C. The difference between the calculated modulus and the

Table AII. Composition of the 42 Alloys and the Reported Measured M_S^z , Driving Force for Transformation at the M_S^z and the Modulus

Source	C	Si	Mn	Al	Cr	Ni	N	M_S^z (K)	$\Delta G^{\gamma \rightarrow \alpha}$ (J/mol)	E (GPa)
Present work	0.086	2.07	13.9	2.01	—	—	0.0116	352 (79)	-1489	168
	0.16	2.97	14.3	0.89	—	—	0.0224	417 (144)	-943	147
	0.06	1.85	14.2	2.38	—	—	0.019	390 (117)	-1310	144
	0.0767	1.95	15.1	1.4	—	—	0.0173	413 (140)	-1076	153
	0.17	2.95	12.5	1.09	—	—	0.0228	354 (81)	-1606	160
	0.1	1.57	13.0	0.45	—	—	0.045	335 (62)	-1811	168
	0.08	2.16	7.82	2.01	0.039	0.93	0.004	505 (232)	-1594	187
	0.078	2.16	7.87	2.44	0.039	1.29	0.003	473 (200)	-1740	211
	0.2	2.15	7.73	2.27	3.02	1.23	0.005	361 (88)	-1785	186
	0.18	3.09	7.9	0.65	—	—	0.024	457 (184)	-1716	175
	0.25	2.66	8.1	2.38	—	—	0.007	428 (155)	-1707	182
	0.11	2.46	11.5	0.38	—	—	0.029	409 (136)	-1575	181
40	0.006	0.01	15.7	—	—	—	—	447 (174)	-1063	176
	0.0023	0.0005	9.28	—	—	—	—	602 (329)	-1185	189
42	0.022	—	10.24	—	8.19	—	0.206	323 (50)	-1763	184
	0.012	—	5.03	—	11.7	—	0.614	257 (-16)	-2829	210
	0.10	2.7	—	—	17	4	—	290 (17)	-2330	201
	0.1	2	—	—	17	4	—	320 (47)	-2230	194
	0.014	—	10.13	—	12.23	—	0.018	384 (111)	-1115	143
	0.06	—	—	—	13	14.2	0.15	183 (-90)	-2011	185
	0.06	—	—	—	11.5	15.1	0.15	173 (-100)	-2075	183
	0.3	—	—	—	9	11	—	253 (-20)	-2085	187
	0.14	—	4.95	—	8.19	—	0.206	489 (216)	-1540	196
	10	—	—	14.8	—	—	—	—	457 (184)	-1063
—		—	11.83	—	—	—	—	492 (219)	-1460	184
—		—	9.85	—	—	—	—	594 (321)	-1149	188
—		—	7.88	—	—	—	—	684 (411)	-892	197
41	—	—	13.7	—	—	—	—	380 (107)	-1815	194
	—	—	10.2	—	—	—	—	480 (207)	-1822	198
39	0.2	1.5	2	—	0.6	—	—	668 (395)	-1371	189
38	0.017	—	0.12	—	8.1	—	0.017	822 (549)	-589	211
	0.017	—	0.12	—	8.1	—	0.206	731 (458)	-1103	204
	0.014	—	4.95	—	7.8	—	0.011	644 (371)	-898	201
	0.014	—	4.95	—	7.8	—	0.258	545 (272)	-1487	193
	0.014	—	4.95	—	7.8	—	0.387	489 (216)	-1829	188
	0.022	—	10.24	—	8.19	—	0.206	331 (58)	-1720	184
	0.008	—	0.094	—	12.5	—	0.257	674 (401)	-1183	185
	0.012	—	5.03	—	11.7	—	0.29	460 (187)	-1662	194
	0.012	—	5.03	—	11.7	—	0.466	396 (123)	-2026	187
	43	0.30	2.0	10.0	3.0	—	—	—	357 (84)	-1711
0.40		2.0	8.00	3.0	—	—	—	355 (82)	-1877	173

measured modulus is fit with a least squares fit for the elements Si, Al, and N.

REFERENCES

1. Q. Li, Xu. Huang, and W. Huang: *Met. Sci. Eng.*, 2016, vol. 662, pp. 129–35.
2. D.C. Van Aken, S.T. Pisarik, and M.C. McGrath: *Proceedings of the Intl. Symp. on New Developments in Advanced High-Strength Steels*, Vail, Colorado. 2013. pp. 119–29.
3. M.C. McGrath, D.C. Van Aken, N.I. Medvedeva, and J.E. Medvedeva: *Metall. Mater. Trans. A*, 2013, vol. 44A, pp. 4634–43.
4. S.T. Pisarik, D.C. Van Aken, K. Limmer, and J.E. Medvedeva: *AIST2014 Proceedings*, pp. 3013–23.
5. A.J. Clark, J.G. Speer, M.K. Miller, R.E. Hackenberg, D.V. Edmonds, D.K. Matlock, F.C. Rizzo, K.D. Clarke, and E. De Moor: *Acta Mater.*, 2008, vol. 56, pp. 16–22.
6. M.J. Santofimia, L. Zhao, and J. Sietsma: *Met. Trans. A*, 2011, vol. 42A, pp. 3620–26.
7. E. De Moor, S. Lacroix, A.J. Clark, J. Penning, and J.G. Speer: *Met. Trans. A.*, 2008, vol. 39A, pp. 2586–95.
8. O. Grassel, G. Frommeyer, C. Derder, and H. Hofmann: *J. Phys. IV France*, 1997, vol. 7, pp. c5-383–88.
9. D.M. Field and D.C. Van Aken: *Met. Trans. A.*, 2016, vol. 47A, pp. 1912–17.
10. M. Acet, T. Schneider, B. Gehrman, and E.F. Wasserman: *J. Phys.*, 1995, vol. 5, pp. 379–84.
11. A. Holden, J.D. Bolton, and E.R. Petty: *J. Iron Steel Inst.*, 1971, vol. 209, pp. 721–28.
12. N.I. Medvedeva, M.S. Park, D.C. Van Aken, and J.E. Medvedeva: *J. Alloys Compd.*, 2014, vol. 582, pp. 475–82.
13. G.R. Speich, A.J. Schwoeble, and W.C. Leslie: *Met. Trans.*, 1972, vol. 3, pp. 2031–37.
14. B.C. De Cooman and J.G. Speer: *Austenite Decomposition in Fe-C-X Alloy Systems, Fundamentals of Steel Product Physical Metallurgy*, 1st ed., ASM International, Materials Park, OH, 2011, p. 173.
15. Z. Jicheng and J. Zhanpeng: *Acta Metall. Mater.*, 1990, vol. 38, pp. 425–31.
16. V. Raghavan and D. Anita: *Metall. Mater. Trans A*, 1996, vol. 27A, pp. 1127–32.
17. K.W. Andrews: *J. Iron Steel Inst.*, 1965, vol. 203, pp. 721–27.
18. A. Stromvinter, A. Borgenstam, and J. Ågren: *Met. Trans. A*, 2012, vol. 43A, pp. 3870–79.
19. M. Palumbo, *Computer Coupling of Phase Diagram and Thermochemistry*, 2008, pp. 693–708.
20. G.B. Olson and M. Cohen: *Met. Trans. A*, 1976, vol. 7, pp. 1905–14.
21. G.B. Olsen and M. Cohen: *Met. Trans. A*, 1976, vol. 7, pp. 1897–1904.
22. S.T. Pisarik and D.C. Van Aken: *Met. Trans. A.*, 2016, vol. 47A, pp. 1009–18.
23. M. Grujcic, G.B. Olson, and W.S. Owen: *Metall. Trans. A.*, 1985, vol. 16A, pp. 1713–22.
24. L. Kaufman and M. Cohen: *Progr. Metal. Phys.*, 1958, vol. 7, pp. 165–246.
25. J.S. Bowles and A.J. Morton: *Acta Metall.*, 1964, vol. 12, pp. 629–37.
26. J.F. Breedis and L. Kaufman: *Metall. Trans.*, 1971, vol. 2, pp. 2359–71.
27. Y.K. Lee and C.S. Choi: *Metall. Mater. Trans A*, 2000, vol. 31A, pp. 355–60.
28. S. Allain, J.P. Chateau, O. Bouaziz, S. Migot, and N. Guelton: *Mater. Sci. Eng. A*, 2004, vols. 387–389, pp. 158–62.
29. W.S. Yang and C.M. Wan: *J. Mater. Sci.*, 1990, vol. 25, pp. 1821–23.
30. S.T. Pisarik, MS thesis, Missouri University of Science and Technology 2014.
31. L. Kaufman: *CALPHAD*, 1978, vol. 2, pp. 295–318.
32. L. Kaufman: *CALPHAD*, 1979, vol. 3, pp. 45–76.
33. L. Kaufman: *CALPHAD*, 1978, vol. 2, pp. 325–48.
34. L. Kaufman: *CALPHAD*, 1978, vol. 2, pp. 117–46.
35. A.T. Disndale: SGTE data for pure elements *CALPHAD*, 1991, vol. 15, pp. 317–425.
36. ASTM E 8/E 8M-08, Standard Test Methods for Tension Testing of Metallic Materials.
37. S. Martin, C. Ullrich, D. Simek, U. Martin, and D. Rafaja: *J. Appl. Crystallogr.*, 2011, vol. 44, pp. 779–87.
38. U.R. Lenel and B.R. Knott: *Met. Trans. A.*, 1987, vol. 18A, pp. 767–75.
39. M.C. Somani, D.A. Porter, L.P. Karjalainen, and R.D.K. Misra: *Met. Trans. A.*, 2014, vol. 45A, pp. 1247–57.
40. K. Tsuzaki, S. Fukasaku, Y. Tomota, and T. Maki: *Mater. Trans.*, 1991, vol. 32, pp. 222–28.
41. S. Cotes, M. Sade, and A.F. Guillermet: *Met. Trans. A.*, 1995, vol. 26A, pp. 1957–69.
42. Q.X. Dai, X.N. Cheng, Y.T. Zhao, X.M. Lou, and Z.Z. Yuan: *Mater. Charact.*, 2004, vol. 52, pp. 349–54.
43. S. Lee and B.C. De Cooman: *Met. Trans. A.*, 2016, vol. 47A, pp. 3263–70.
44. G. Ghosh and G.B. Olson: *Acta Mater.*, 2002, vol. 50, pp. 2655–75.
45. S. Takeuchi: *J. Phys. Soc. Jpn.*, 1969, vol. 27, p. 929.
46. G. Ghosh and G.B. Olson: *Acta Mater.*, 1993, vol. 42, pp. 3361–70.
47. S.T. Pisarik and D.C. Van Aken: *Met. Trans. A.*, 2014, vol. 45, pp. 3173–78.
48. M. Atkins: *Atlas of continuous cooling transformation diagrams for engineering steels*, ASM, (1980).
49. E. Yang, H. Zurob, and J. McDermid: *Proc. of MS&T'10*, 2010, pp. 438–46.
50. J.-C. Kim, D.-W. Han, S.-H. Baik, and Y.-K. Lee: *Mater. Sci. Eng.*, 2004, vol. 378, pp. 323–27.
51. K.R. Limmer, J.E. Medvedeva, D.C. Van Aken, and N.I. Medvedeva: *Comput. Mater. Sci.*, 2015, vol. 99, pp. 253–55.
52. P.R. Swann: *Corrosion*, 1963, vol. 19, p. 102.
53. R.E. Schramm and R.P. Reed: *Metall. Trans. A*, 1975, vol. 6A, p. 1345.
54. L.M. Kaputkina, V.G. Prokoshkina, and N.A. Krysinina: *Metals*, 2001, vol. 6, p. 80.
55. T. De Cock, C. Capdevila, F.G. Caballero, and C. Garcia de Andres: *Scripta Mater.*, 2006, vol. 54, pp. 949–54.
56. H.S. Yang, J.H. Jang, H.K.D.H. Bhadeshia, and D.W. Suh: *CALPHAD*, 2012, vol. 36, pp. 16–22.
57. J.H. Jun and C.S. Choi: *Mater. Sci. Eng. A*, 1998, vol. 257, pp. 535–556.
58. S. Takaki, H. Nakatsu, and T. Tokunaga: *Mater. Trans. JIM*, 1993, vol. 34, pp. 489–95.
59. P.Y. Volosevich, V.N. Gridnev, and Y.N. Petrov: *Phys. Met. Metallogr.*, 1975, vol. 40, pp. 554–59.